

A Node-Based Polar List Decoder with Frame Interleaving and Ensemble Decoding Support

Yuqing Ren, Leyu Zhang, Ludovic Damien Blanc, Yifei Shen, Xinwei Li,
Alexios Balatsoukas-Stimming, Chuan Zhang, Andreas Burg

Abstract—Node-based successive cancellation list (SCL) decoding has received considerable attention in wireless communications for its significant reduction in decoding latency, particularly with 5G New Radio (NR) polar codes. However, the existing node-based SCL decoders are constrained by sequential processing, leading to complicated and data-dependent computational units that introduce unavoidable stalls, reducing hardware efficiency. In this paper, we present a frame-interleaving hardware architecture for a generalized node-based SCL decoder. By efficiently reusing otherwise idle computational units, two independent frames can be decoded simultaneously, resulting in a significant throughput gain. Based on this new architecture, we further exploit graph ensembles to diversify the decoding space, thus enhancing the error-correcting performance with a limited list size. Two dynamic strategies are proposed to eliminate the residual stalls in the decoding schedule, which eventually results in nearly $2\times$ throughput compared to the state-of-the-art baseline node-based SCL decoder. To impart the decoder rate flexibility, we develop a novel online instruction generator to identify the generalized nodes and produce instructions on-the-fly. The corresponding 28nm FD-SOI ASIC SCL decoder with a list size of 8 has a core area of 1.28 mm^2 and operates at 692 MHz. It is compatible with all 5G NR polar codes and achieves a throughput of 3.34 Gbps and an area efficiency of 2.62 Gbps/mm^2 for uplink (1024, 512) codes, which is $1.41\times$ and $1.69\times$ better than the state-of-the-art node-based SCL decoders.

Index Terms—Polar codes, successive cancellation list (SCL) decoder, frame-interleaving, sequence repetition (SR) node, hardware architecture, graph ensembles, 5G.

I. INTRODUCTION

POLAR codes [1] have been ratified as the standard codes to protect control channels in 5G enhanced mobile broadband (eMBB) [2], thus raising significant attention in both academia and industry. Successive cancellation (SC) [1] and SC list (SCL) decoding [3] led the mainstream development of polar decoding algorithms and implementations. In particular, SCL decoding can evaluate two hypotheses for each information bit, by estimating each information bit as either 0 or 1 and maintaining a list of up to L candidate codewords in parallel during the decoding. This yields superior

error-correcting performance compared to SC decoding. Using hardware-friendly log-likelihood ratio (LLR)-based SCL decoding [4], an SCL decoder with $L = 8$ provides a good trade-off between error-correcting performance and hardware complexity and has been chosen as the algorithm baseline during the 5G standardization process [5].

In terms of hardware implementation, to reduce long decoding latency in conventional SC-based decoders [4], [6], node-based techniques have been introduced to SC decoders [7]–[9], in which special bit patterns of constituent codes can be identified in the decoding tree to allow direct decoding of multiple bits in parallel instead of repeatedly traversing the corresponding parts of the tree. Then, such techniques were also introduced to SCL decoders, using list extension strategies for special nodes [10]–[12], thereby significantly decreasing the decoding latency. Notably, the recently found generalized sequence repetition node (SR) [13] can support most existing node patterns in SC decoding. The work in [14] first extends the SR node to SCL decoding and implements a corresponding SR-List decoder to meet the stringent low-latency and low-complexity requirements of 5G. However, the existing SCL decoders (including [14]) still suffer from sequential processing in the special nodes, which leads to unavoidable stalls. To mitigate the impact of these stalls, based on the architecture in [11], several latency-optimization techniques have been proposed in [15] to reduce idle cycles by modifying the architectures of computational units to allow for overlapped processing.

In addition to low latency, high reliability is also essential, but the error-correcting capability of SCL decoding, with a limited list size, falls short in some resource-constrained scenarios and demands further enhancement. Recently, automorphism ensemble decoding (AED) gained a lot of attention due to its superior performance and universality [16]–[19]. AED employs code automorphisms, represented as a block lower triangular affine (BLTA) group in polar codes [16], to decode various codeword permutations in parallel, demonstrating particular effectiveness for short-length polar codes [18]. However, its hard-wired routing of permutations lacks flexibility for diverse automorphisms. It is noteworthy that as a subset of a general affine (GA) group, factor graph permutations [20], [21] (also known as permuted factor graphs, PFGs) efficiently widen the decoding space through graph ensemble decoding and can be implemented in hardware to generate these permuted graphs on-the-fly [22]. However, this factor graph permutation alters the bit indices [23] and thus greatly affects the node structure of the polar decoding tree. This alteration complicates the direct application of node techniques

Y. Ren, L. D. Blanc, Y. Shen, X. Li and A. Burg are with the Telecommunications Circuits Laboratory, École Polytechnique Fédérale de Lausanne (EPFL), Lausanne 1015, Switzerland. (Yuqing Ren and Leyu Zhang equally contributed to this work. Corresponding author: Andreas Burg)

L. Zhang is with the Telecommunications Circuits Laboratory, École Polytechnique Fédérale de Lausanne (EPFL), Lausanne 1015, Switzerland and also with the CAS Key Laboratory of Wireless-Optical Communications, University of Science and Technology of China (USTC), China.

A. Balatsoukas-Stimming is with the Department of Electrical Engineering, Eindhoven University of Technology, 5600 MB Eindhoven, The Netherlands.

C. Zhang is with the Lab of Efficient Architectures for Digital-communication and Signal-processing (LEADS), Southeast University, China.

to graph ensemble decoding. Therefore, integrating graph ensembles with SCL decoding and node-based techniques for high performance and low latency remains challenging.

Moreover, these node-based polar decoders rely on the identification of the type and the length of special codes, which necessitates complex control logic [7]. To bypass this issue, most decoders generate instructions offline and store the resulting instructions in dedicated memories. The decoder then proceeds by reading these instructions to coordinate each component. However, this instruction storage incurs significant area overhead [7], [11], [24]. Given the wide range of message lengths from 12 to 1706 in 5G NR polar codes, it is impractical to store all possibilities and a rapid succession of code changes leaves no time to generate instructions. To overcome this issue, an online generator is proposed in [25] to identify the special patterns of basic nodes directly in hardware based on the channel relative reliability vector, thus supporting a rate-flexible decoder. However, to the best knowledge of the authors, there is currently no online generator compatible with more generalized nodes, such as SR nodes, that achieves both strict low decoding latency and rate flexibility in generalized node-based SCL decoders.

Contributions:

This work is an extension of our work in [26], in which the node-based SCL decoder with frame-interleaving was initially proposed. However, due to the mismatch in the processing cycles of computational units, some inevitable stalls still exist and they degrade throughput and area efficiency improvements [26]. Moreover, the decoder from [26] relies on storing offline-generated instructions, which compromises its rate flexibility. In this paper, we enhance the generalized node-based SCL decoder with frame-interleaving to address the above issues while remaining compatible with all 5G NR polar codes. Our contributions comprise the following:

- 1) We propose a node-based SCL decoder with frame-interleaving, based on which, two independent frames can be decoded simultaneously by reusing the computational units in an alternating fashion. This architecture significantly enhances the throughput at the cost of a small area increment. Moreover, our decoder has three working modes: *Mode-I Frame-Interleaving* tailored to low latency, *Mode-II Graph-Interleaving* tailored to high performance, and *Mode-III Hybrid-Interleaving* tailored to high efficiency.
- 2) To effectively eliminate the residual stalls in the interleaving schedule, we provide two dynamic strategies: overlapped processing of SR nodes and dynamic path forking for high-rate nodes. Based on these two strategies, our decoder can ultimately reduce 49% of decoding cycles (the ideal is 50%) with negligible to no performance degradation.
- 3) We design an online instruction generator that allows the identification of SR nodes from the binary sequence that specifies the information set and generates the list of decoder instructions on-the-fly. Compared to a straightforward instruction memory, our online instruction generator

yields a 97.5% smaller area even for a single code and imparts the proposed SCL decoder rate flexibility.

- 4) We implement the above frame-interleaving node-based SCL decoder, compatible with 5G NR polar codes. The 28nm FD-SOI post-layout implementation has a core area of 1.28 mm², achieves a throughput of 3.34 Gbps at 692 MHz, and has an energy consumption of 60.32 pJ/bit with a supply voltage of 1.0 V.

The remainder of this paper is organized as follows: Section II provides symbol definitions and background on polar codes and decoding. Section III introduces the proposed architecture with frame-interleaving and three working modes. In Section IV, we present two optimization schemes to further reduce the latency. Section V presents a novel online instruction generator which is compatible with basic nodes and SR nodes. Section VI discusses the implementation results and compares them with other works. Section VII concludes the paper.

II. PRELIMINARIES

Notation: Throughout this paper, we follow the definitions introduced below. Boldface lowercase letters \mathbf{u} denote vectors, where $\mathbf{u}[i]$ refers to the i -th element of \mathbf{u} and $\mathbf{u}[i : j]$ is the sub-vector $(\mathbf{u}[i], \mathbf{u}[i + 1], \dots, \mathbf{u}[j])$, $i \leq j$ and the null vector otherwise. Boldface uppercase letters \mathbf{B} represent matrices, where $\mathbf{B}[i][j]$ denotes the element at the i -th row and j -th column of \mathbf{B} . Blackboard letters \mathbb{S} mean sets with $|\mathbb{S}|$ being the cardinality. We adopt the following parameters from the 5G NR standard [27]: $N = 2^n$ is the length of the mother polar code, K is the number of message bits, $K' = K + P$ is the number of information bits with length- P CRC bits, and E the length of the codeword after rate-matching. We denote a 5G NR polar code as (E, K) , and the corresponding frozen and information sets are defined as \mathbb{F} and \mathbb{A} . For brevity, we use uplink (UL) and downlink (DL) polar codes from 5G NR. More detailed formulation of the information set and rate-matching principles for 5G NR polar codes are described in [2]. We use one *frame* to describe one codeword during the transmission. Note that all indices regarding decoding start from 0.

A. Construction and Encoding

Given a length- N input bit sequence \mathbf{u} , the encoded vector \mathbf{x} is generated by $\mathbf{x} = \mathbf{u} \cdot \mathbf{G}$, where $\mathbf{G} = \mathbf{F}^{\otimes n}$ is the n -fold Kronecker product of $\mathbf{F} = \begin{bmatrix} 1 & 0 \\ 1 & 1 \end{bmatrix}$. Based on the principle of channel polarization [1], the K' most reliable bit channels transmit information bits along with CRC bits, while the remaining $N - K'$ bit channels transmit frozen bits, typically set to a value of 0. The \mathbf{G} -based factor graph of length- N polar codes is called the original factor graph (OFG), defined as π_* including $n + 1$ stages. Given a graph permutation, we represent any PFG as π , and the design space is π which contains $|\pi| = n! - 1$ possible PFGs.

B. SC and SCL Decoding

SC decoding can be represented as the traversal over a binary decoding tree with $n + 1$ stages, where SC decoding

successively updates the bit likelihoods. Let $\mathcal{N}_{s,i}$ denote the i -th node (the node length is 2^s) at stage s , where $0 \leq i < 2^{n-s}$ and $0 \leq s \leq n$. For $\mathcal{N}_{s,i}$, a length- 2^s LLR vector $\lambda_{s,i}$ is received and after traversing all the child nodes, the node returns a length- 2^s partial sum (PSUM) vector $\beta_{s,i}$. The detailed update rules are described in (1)

$$\begin{aligned}\lambda_{s,2i}[j] &= f(\lambda_{s+1,i}[j], \lambda_{s+1,i}[j+2^s]), \\ \lambda_{s,2i+1}[j] &= g(\lambda_{s+1,i}[j], \lambda_{s+1,i}[j+2^s], \beta_{s,2i}[j]),\end{aligned}\quad (1)$$

where f - and g -functions are defined in (2).

$$\begin{aligned}f(x, y) &\approx \text{sgn}(x) \text{sgn}(y) \min\{|x|, |y|\}, \\ g(x, y, z) &= (1 - 2z)x + y.\end{aligned}\quad (2)$$

The update rule for PSUM is shown in (3).

$$\begin{aligned}\beta_{s+1,i}[j] &= \beta_{s,2i}[j] \oplus \beta_{s,2i+1}[j], \\ \beta_{s+1,i}[j+2^s] &= \beta_{s,2i+1}[j].\end{aligned}\quad (3)$$

To mitigate the serial error propagation caused by bit errors in SC decoding, SCL decoding applies a breadth-first search to identify promising candidate codewords in the decoding tree. At the cost of higher storage and computing complexity to enhance reliability, SCL decoding maintains a list of up to L paths by examining both hypotheses for each information bit. The reliabilities of the path candidates are measured by a path metric (PM) [4], which is calculated as

$$\text{PM}_i^{(l)} \approx \begin{cases} \text{PM}_{i-1}^{(l)} + |\lambda_{0,i}^{(l)}|, & \text{if } \hat{u}[i] \neq \text{HD}(\lambda_{0,i}^{(l)}), \\ \text{PM}_{i-1}^{(l)}, & \text{otherwise.} \end{cases}\quad (4)$$

Here $\text{PM}_i^{(l)}$ denotes the PM of the l -th path after obtaining the estimated value $\hat{u}[i]$ of the i -th bit, where $0 \leq l < L$, $0 \leq i < N$. The hard decision function is defined as $\text{HD}(x) = 1$ if $x < 0$ and $\text{HD}(x) = 0$ if $x \geq 0$. We refer to the process of splitting a partial candidate codeword into two candidates by considering both the 0 and 1 hypotheses for the current bit as *path forking*. Only up to L paths with the smallest PM values are retained after each path forking.

C. Node-Based Decoding

To mitigate the huge latency when traversing the bottom of the decoding tree in SC and SCL decoding, special nodes identified by their distinct frozen bit patterns, as proposed in [7]–[9], enable the direct computation of the PSUM vector β using tailored decoding algorithms. To label whether a leaf bit in the fanout tree of a node $\mathcal{N}_{s,i}$ is frozen, we use a binary vector $\mathbf{d}_{s,i}$, where $\mathbf{d}_{s,i}[j] = 0$ indicates a frozen bit and an information bit otherwise. Following the constraints of [14], we consider five types of basic nodes whose vectors \mathbf{d}_s are listed below.

- 1) **R0** $\mathbf{d}_s = (0, 0, 0, \dots, 0, 0)$
- 2) **R1** $\mathbf{d}_s = (1, 1, 1, \dots, 1, 1)$
- 3) **REP** $\mathbf{d}_s = (0, 0, 0, \dots, 0, 1)$
- 4) **SPC** $\mathbf{d}_s = (0, 1, 1, \dots, 1, 1)$
- 5) **TYPE-III** $\mathbf{d}_s = (0, 0, 1, \dots, 1, 1)$

Furthermore, the recent generalized SR node [13] includes most existing nodes as its special cases. An SR node at stage

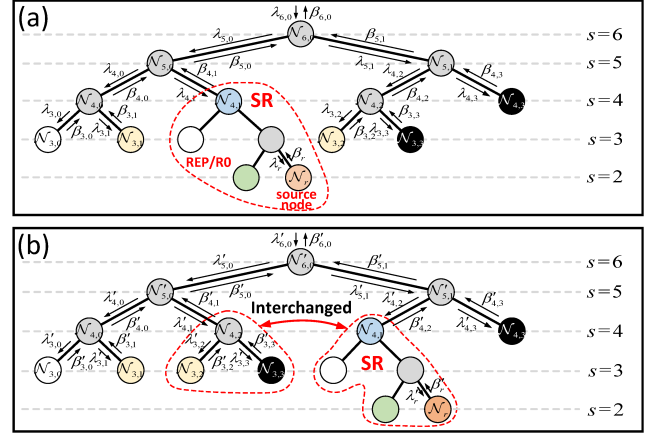


Fig. 1. (a) Decoding tree for $N = 64$ polar codes with special nodes. (b) Decoding tree after factor graph permutation for $N = 64$ polar codes. The node types are \circ for R0, \bullet for REP, \bullet for R1, \bullet for SPC, \bullet for TYPE-III, \bullet for SR, and \bullet for a node of any rate. The superscript ' indicates that the vectors λ s and β s are permuted.

Algorithm 1: SCL Decoding with PFGs()

```

1 Input:  $\lambda_{n,0}, \mathbb{A}, \mathbb{P}$ 
2  $\hat{\mathbf{u}} \leftarrow \text{SCLdecoding}(\lambda_{n,0}, \mathbb{A});$ 
3 if CRCdetection( $\hat{\mathbf{u}}$ ) == 1 then
4   for  $i = 1$  to  $|\mathbb{P}| - 1$  do
5      $[\lambda'_{n,0}, \mathbb{A}'] \leftarrow \text{permutation}(\lambda_{n,0}, \mathbb{A}, \pi_i);$ 
6      $\hat{\mathbf{u}}' \leftarrow \text{SCLdecoding}(\lambda'_{n,0}, \mathbb{A}');$ 
7      $\hat{\mathbf{u}} \leftarrow \text{permutationReverse}(\hat{\mathbf{u}}', \pi_i);$ 
8     if CRCdetection( $\hat{\mathbf{u}}$ ) == 0 then
9       break;
10 return  $\hat{\mathbf{u}};$ 

```

s consists of $s - r$ R0/REP nodes as its left descendants and a source node of any type as its last right-descendant located at lower stage r , where $r < s$. Its pattern is shown in (5), where each “X” can be either a frozen or an information bit.

$$\mathbf{d}_s = (\underbrace{0, \dots, 0}_{2^{s-1}}, \underbrace{0, \dots, 0}_{2^r}, \underbrace{X, X, \dots, X}_{2^r}) \quad (5)$$

As depicted in Fig. 1(a), $\mathcal{N}_{4,1}$ is an SR node that consists of two R0/REP nodes across stages 2 to 3 and a TYPE-III node as its source node \mathcal{N}_r at stage 2. For brevity, we use SR(SNT) to describe an SR node, where SNT is the high-rate source node type restricted to R1, SPC, and TYPE-III in this work [14]. Assume that there exist W R0/REP nodes in an SR node, $\mathbb{S} = \{\mathbb{S}_0, \mathbb{S}_1, \dots, \mathbb{S}_{2^W-1}\}$ denotes the set of all $|\mathbb{S}|$ possible repetition sequences for a given SR node. It is noteworthy that thanks to its significant parallelism, the decoding of SR nodes provides low latency [13] and facilitates efficient hardware implementations of SCL decoding in 5G as shown in [14].

D. Decoding with Permuted Factor Graphs

Decoding on PFGs can widen the codeword search space to further enhance the error-correcting capability of SCL decoding when the list size is constrained [28]. Note that the codeword permutation proposed in [23] reveals the one-to-one mapping between the permutation of factor graph

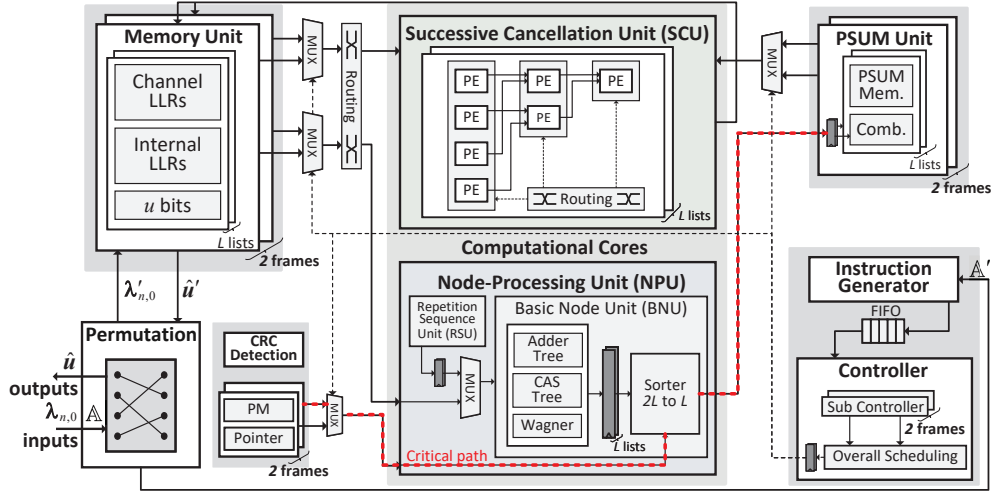


Fig. 2. Top-level overview of the proposed SCL decoder with interleaving architecture, where the red dotted lines show the critical path.

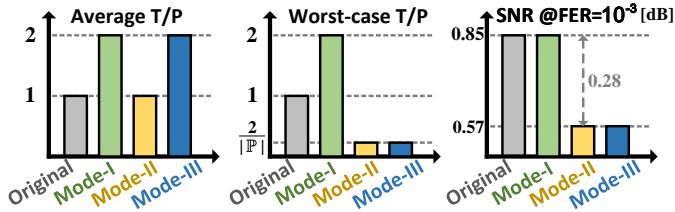


Fig. 3. Comparison between the baseline decoder [14] and our frame-interleaving SCL decoder operating in various modes for DL-(432, 140) code using SCL-8 decoding with $|\mathbb{P}| = 8$.

stages and the shuffling of bit indices in a codeword. This enables the decoder to reuse its original architecture by merely shuffling the input LLRs to realize decoding on PFGs. This idea has been implemented in the belief propagation list (BPL) decoder in [22]. Herein, we outline the sequential processing of SCL decoding on multiple PFGs in Algorithm 1. Given that the OFG π_* always yields the best average error-correcting performance [23], [29], the first decoding attempt is identical to the original SCL without any permutation. If decoding fails to satisfy the CRC, a codeword permutation is carried out to generate the permuted input LLRs $\lambda'_{n,0}$ as well as the corresponding information set \mathbb{A}' shown in Fig. 1(b), based on which the permuted SCL decoding is executed. Let \mathbb{P} denote the ensemble of $|\mathbb{P}|$ graph candidates, including π_* as its first element and $|\mathbb{P}| - 1$ PFGs. Once a decoding attempt passes the CRC detection, the decoded results are output. Otherwise, the next attempt on a new PFG is scheduled until a valid codeword is generated or all the candidates in \mathbb{P} are exhausted.

III. HARDWARE ARCHITECTURE FOR NODE-BASED SCL DECODER WITH FRAME-INTERLEAVING

Node-based decoding generally relies on two primary operations, which are mapped to two distinct hardware units in the decoder: a SC unit (SCU) for the internal LLR calculation and a node-processing unit (NPU) for fast node decoding. However, due to the data dependency inherent in sequential

processing, these two units must work in an alternating fashion. Specifically, the NPU needs to wait until the SCU has computed the required LLR vector λ . Similarly, the SCU requires the updated PSUM vector β from the NPU before proceeding. This sequential invocation always leaves one computational unit idle when the other one is running, limiting the hardware utilization and throughput. In this section, we present a new node-based SCL decoder with a frame-interleaving architecture shown in Fig. 2 to fill the resulting idle slots with another frame, thereby significantly enhancing hardware utilization. Moreover, our decoder has three different working modes: Mode-I Frame-Interleaving tailored to low latency, Mode-II Graph-Interleaving tailored to high performance, and Mode-III Hybrid-Interleaving (a mixture of the above two modes) tailored to high efficiency. It is noteworthy that the internal controller can easily switch between these three modes. Implementation results shown in Fig. 3 demonstrate that our frame-interleaving SCL decoder operating across various modes has advantages in average throughput, worst-case throughput, and reliability compared to the baseline decoder [14]. This frame-interleaving architecture is especially useful for the blind decoding and detection required for 5G where the received data must be decoded multiple times speculating on the transmit/encoding parameters [30]. It is further useful for high-throughput data channels where after a short initial latency, two frames can be decoded in almost the same time as a single frame with a non-interleaved decoder.

A. Top-Level Hardware Architecture

In Fig. 2, we present a top-level illustration of our SCL decoder with interleaving architecture. This architecture comprises four main types of modules: computational cores, memories, a permutation generator [22], and a controller with an online instruction generator. Since we intend to process two independent frames concurrently in an interleaved fashion, storage (memories) in the decoder must be duplicated, including channel LLRs, internal LLRs, output bits, PSUMs, pointers, and PMs. The computational cores (i.e., the SCU and

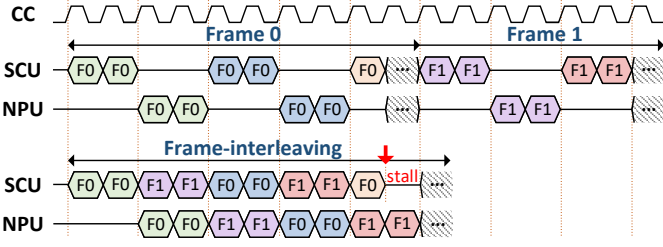


Fig. 4. Decoding schedules of two frames using conventional single-frame architecture and our interleaving architecture, where the i -th frame is denoted as F_i . Operations on different nodes are marked by distinct colors for clarity.

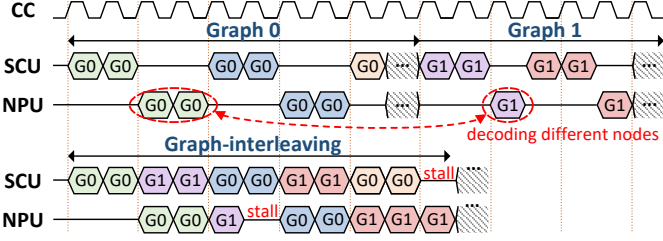


Fig. 5. Decoding schedules of two graphs on the same frame using conventional single-frame architecture and our interleaving architecture, where the i -th graph is denoted as G_i .

the NPU) read channel or internal LLRs from the memory unit to calculate the vectors λ s and β s, respectively. Specifically, the SCU is implemented by multiple stages of processing elements (PEs) [31] to calculate the internal LLRs λ (referring to (1)), processing several stages of the decoding tree in a single cycle. This technique can significantly reduce the internal LLR memory overhead since intermediate LLRs are re-calculated combinatorially without being stored [31]. Note that the SCU operation continues until a special node is encountered, and the resulting LLRs λ are then passed to the NPU for node-based operations. Meanwhile, to support list decoding for SR nodes [14], the NPU instantiates two core units, a repetition sequence unit (RSU) for the low-rate part of SR nodes (enumerates all possibilities and then performs $|S|L \rightarrow L$ sorting) and a basic node unit (BNU) for the high-rate source node (sequentially runs multiple $2L \rightarrow L$ path forking). The BNU consists of an adder tree, a compare-and-select (CAS) tree, a Wagner decoder for parity check, and a $2L$ -to- L sorter for path forking [4]. Note that the processing of a single node can take multiple clock cycles (CCs), which is discussed further in Section IV.

Our frame-interleaving architecture time-shares the two computational units (the SCU and the NPU) between two independent frames. We denote them as Frame 0 and Frame 1 for brevity. Given that the SCU and the NPU typically occupy more than half of the area [14], time-sharing these computational units offers an obvious area advantage for our interleaving architecture, compared to a simple instantiation of two parallel decoders (multiple cores). While the SCU is calculating LLRs for Frame 0, the NPU performs node list decoding for Frame 1 and vice versa. The controller generates the control logic to determine whether to read the data for either Frame 0 or Frame 1, which contains two

sub-controllers and a scheduling unit. Two sub-controllers orchestrate the decoding process of two frames independently, and the scheduling unit is responsible for the hand-shaking among two sub-controllers and the datapath components of the decoder. An online instruction generator avoids the need for a memory to store all offline-generated instructions (e.g., in the non-interleaving baseline SCL decoder [14]). This generator can identify the node patterns (including SR nodes) for any given information set and delivers a list of instructions on the fly, greatly enhancing the flexibility of our SCL decoder and reducing the area overhead of the instruction memory. We describe it in detail in Section V.

B. Timing and Operation Schedules for Different Modes

In this section, we give example timing diagrams to clearly illustrate the scheduling of our three working modes.¹

1) *Mode-I Frame-Interleaving*: In this mode, we interleave two frames to fill the unused slots in the SCU and the NPU while waiting for the other unit to complete its operation. As illustrated in Fig. 4, the decoding process of Frame 1 is moved forward and integrated into the idle cycles caused by Frame 0. Ideally, both frames proceed in a fully pipelined manner without any idle cycles of the SCU and the NPU. Yet, in practice, some inevitable stalls occur due to the mismatch in the number of processing cycles of the SCU and the NPU. For length-432 DL polar codes, the average and worst-case number of residual stalls in Mode-I are 21.3 and 29 cycles, respectively. For length-1024 UL polar codes, these numbers increase to 58.3 and 78 cycles, respectively. For example, as shown by the red arrow in Fig. 4, Frame 0 finishes the λ calculation and then asserts the request signal to the NPU. The overall scheduling unit (shown in Fig. 2) performs hand-shaking operations with the NPU, but discovers that it is busy processing Frame 1. Hence, Frame 0 has to wait until the NPU is idle, thus leading to a stall. Nevertheless, the resulting stalls are much fewer than those in the traditional single-frame decoder, thereby resulting in better hardware utilization as well as higher (both average and worst-case) throughput.

2) *Mode-II Graph-Interleaving*: Our decoder can employ graph permutations on the same codeword to widen the decoding search space. As mentioned in Section II-D, decoding on PFGs can further enhance the error-correcting capability of the SCL decoder with a constrained list size. This is similar to AED [17], but we only utilize factor graph permutation [20], [21], a subset of the GA group [32] that can be implemented efficiently in hardware [22]. To balance hardware efficiency and throughput, rather than instantiating multiple sub-decoders like [19], we implement a serial decoding scheme that shuffles the input LLRs and reuses a single decoder [22], [23] with frame-interleaving, as outlined in Algorithm 1. While the serial scheme suffers from a longer worst-case decoding latency (increasing proportionally with $|\mathbb{P}|$), our decoder can deliver the same error rate as the parallel scheme [19] at a minor cost of additional area for permutation generation.

¹Note that the PSUM unit (PSU) consistently consumes one cycle to execute (3) after the NPU processing [14]. For brevity, this cycle is conceptually integrated into the SCU processing time for the subsequent node. This allows us to focus on the SCU and the NPU as the primary time-consuming units.

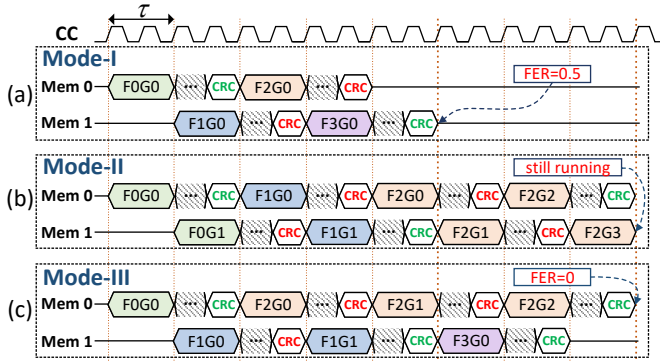


Fig. 6. Decoding schedules of three working modes from the perspective of the memory occupation, where the i -th frame on the j -th graph is denoted as F_iG_j . Herein, operations on different frames are marked by distinct colors. The green CRC represents the CRC check succeeds otherwise labeled as red.

For each graph, we adopt a flexible permutation generator [22] to shuffle the information set \mathbb{A} and the input LLRs of each frame. Note that the shuffling of the input LLRs alters the bit indices within the factor graph and consequently greatly affects the node structure of the decoding tree [23], [28]. Unfortunately, this alternation generally complicates the direct application of node techniques to graph ensemble decoding. However, inspired by [17], we can perform a partially ordered codeword permutation to retain the underlying node structures. Specifically, when permuting the decoding tree (factor graph), we maintain the bottom stages fixed but only permute the upper stages of the decoding tree. This approach can effectively combine the advantages of both graph ensemble decoding and node-based fast decoding.

For instance, Fig. 1(b) illustrates an example of a permuted decoding tree, where the lower four stages are fixed. Bit indices are exchanged in groups of length $2^4 = 16$ while the internal order within each group is not disrupted. Compared to the original decoding tree, two nodes at stage $s = 4$ swap positions accordingly in the permuted tree, marked as $\mathcal{N}_{4,1} \leftrightarrow \mathcal{N}_{4,2}$. It is noteworthy that if we consider graph ensemble decoding as decoding multiple frames containing the same set of special nodes, but shuffled in their order, a “graph” can be naturally regarded as a “frame” for our frame-interleaving decoder. In Fig. 5, the proposed architecture can thus process two graphs for the same frame simultaneously to notably reduce the worst-case latency in the graph-interleaving mode.

3) *Mode-III Hybrid-Interleaving*: Mode-III merges the benefits of both Mode-I and Mode-II. Fig. 6 illustrates the memory occupation for these modes.² Let Mem 0 and Mem 1 denote two separate memory instances in the proposed architecture. As mentioned in Section III-B1, Mode-I focuses on decoder throughput improvement rather than better error-correcting performance. It thus only continuously interleaves two distinct frames on the OFG without using any other PFGs. Notably,

²In our decoder, one cycle is necessary for the CRC detection. Besides, the shuffling of input LLRs will not introduce additional delays as the permutations shown in Fig. 2 and the decoder operate in a fully pipelined fashion. Specifically, while the decoder processes SCL decoding on π_i , the permutation generator is already preparing the next permutation π_{i+1} [22].

$F1G0$ must wait for several cycles until $F0G0$ completes the LLR calculation for the first node and then releases the SCU. For the sake of generality, we assume this stall lasts τ cycles. Conversely, Mode-II prioritizes reducing the error rate through graph ensemble decoding by interleaving as many graphs as possible. Nevertheless, as most erroneous frames in the medium to high SNR region are corrected by the OFG, there are many parallel redundant attempts in Mode-II. For instance, our decoder launches $F0G0$ and $F0G1$ simultaneously in Fig. 6, yet, as $F0G0$ passes the CRC detection while $F0G1$ fails, the decoding attempt on $F0G1$ was effectively useless. Therefore, while Mode-II delivers superior reliability than Mode-I by allowing for up to $|\mathbb{P}|$ additional decoding attempts, its *average throughput* is slightly less than half of Mode-I and approximately identical to the baseline decoder.

To address this issue, we modify the decoding schedule and propose Mode-III (hybrid-interleaving) as a mixture of the above two modes. Two features of Mode-III are summarized as: ① decoding two distinct frames at any one time; ② switching to the next graph only if the current decoding attempt fails. We give priority to executing frame-interleaving and allow for additional decoding attempts on more graphs only when needed. As illustrated in Fig. 6(c), similar to Mode-I, we first decode $F0G0$ and $F1G0$. Once $F0G0$ succeeds, decoding on $F2G0$ is launched. Only when $F1G0$ fails, an additional attempt for the current frame on $G1$ is required. Note that in this case, the order of sequential decoding outputs cannot be guaranteed (e.g., $F3$ outputs before $F2$ in Fig. 6(c)) due to the fact that some frames may need time-consuming serial decoding attempts on more graphs to derive a valid result.

Fig. 3 provides a comparison between our proposed decoder with three interleaving modes and the baseline decoder [14] in terms of the average throughput, the worst-case throughput, and the SNR at the target of 10^{-3} . In ideal scenarios without any stalls (i.e., no mismatch between the SCU and the NPU), Mode-I and Mode-III enjoy a $2\times$ average throughput compared to [14]. However, Mode-II has no improvement in this aspect due to the unnecessary decoding attempts mentioned above. Besides, serial graph ensemble decoding also impairs the worst-case latency, thus leading to a $|\mathbb{P}|\times$ latency increase. Nevertheless, thanks to the proposed interleaving architecture, Mode-II and Mode-III halve the worst-case latency by decoding two graphs simultaneously, resulting in a $\frac{2}{|\mathbb{P}|}\times$ worst-case throughput compared to the baseline decoder [14]. Notably, a significant error-correcting performance gain is achieved by Mode-II and Mode-III. For DL-(432, 140) code, the SNR at the target of 10^{-3} is lowered by 0.28 dB using SCL-8 decoding with $|\mathbb{P}| = 8$. In summary, Mode-III showcases the advantages in both average throughput and reliability, which renders it a preferable operating pattern based on the proposed architecture.

IV. METHODS FOR ELIMINATING REMAINING STALLS IN THE INTERLEAVING SCHEDULE

Ideally, the proposed architecture time-shares two computational units and fills all the idle slots with another frame (or graph) to enhance hardware utilization by $2\times$. However,

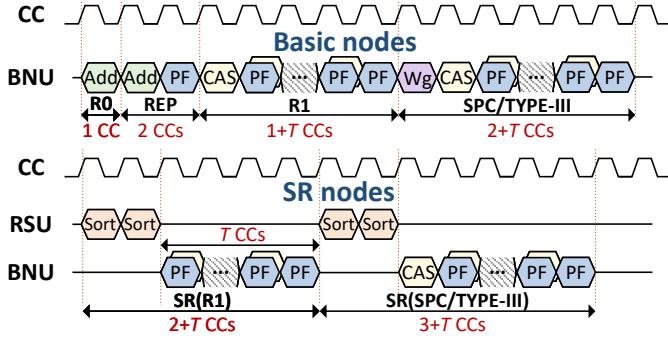


Fig. 7. Cycle-level analysis of node-based decoding for basic and SR nodes [14]. The terms Add, PF, and Wg represent the addition, path forking, and Wagner decoding, respectively.

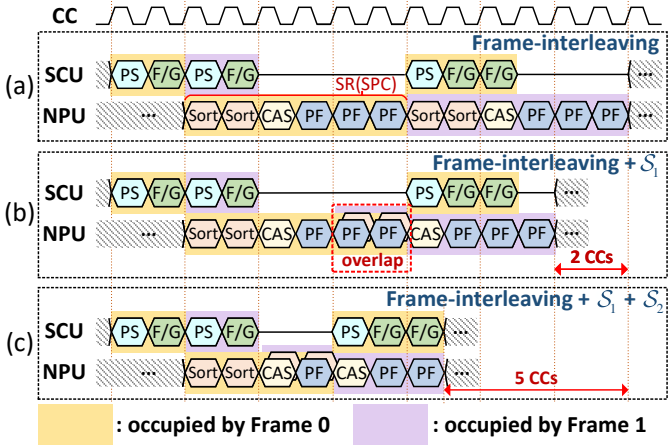


Fig. 8. Decoding schedule of our frame-interleaving decoder adopting two stall-eliminating strategies. The terms PS and F/G represent the PSUM combine and the input LLR calculation of special nodes, respectively.

as mentioned in Section III-B, the unavoidable stalls from the mismatch in the processing cycles of the SCU and the NPU remain, which is a significant challenge. The dominating mismatch pattern arises from the necessity for the SCU to idle while waiting for the NPU to decode high-rate nodes. This NPU process can be time-consuming as it sequentially executes multiple $2L \rightarrow L$ path forking steps. In this context, we present two strategies (S_1 and S_2) to eliminate these remaining stalls. Note that both S_1 and S_2 only require changes of control signals, which is more convenient than [15] to realize overlapped operations and avoid altering the architectures of computational units.

A. Cycle-Level Analysis of the Node-Based Processing

In this section, we first recall the detailed schedule of the NPU running fast list decoding for distinct nodes, as shown in Fig. 7. For R0 and REP nodes, an adder tree takes one CC to compute the PM increment, while the path forking of the single information bit costs an additional cycle in REP nodes. For high-rate nodes, sequential path forking is executed in ascending order of the reliability of the information bits ($|\lambda_s[i]|, i \in [0, 2^s - 1]$). To balance decoding latency and error rate in this decoder, we empirically assign a constraint T to the

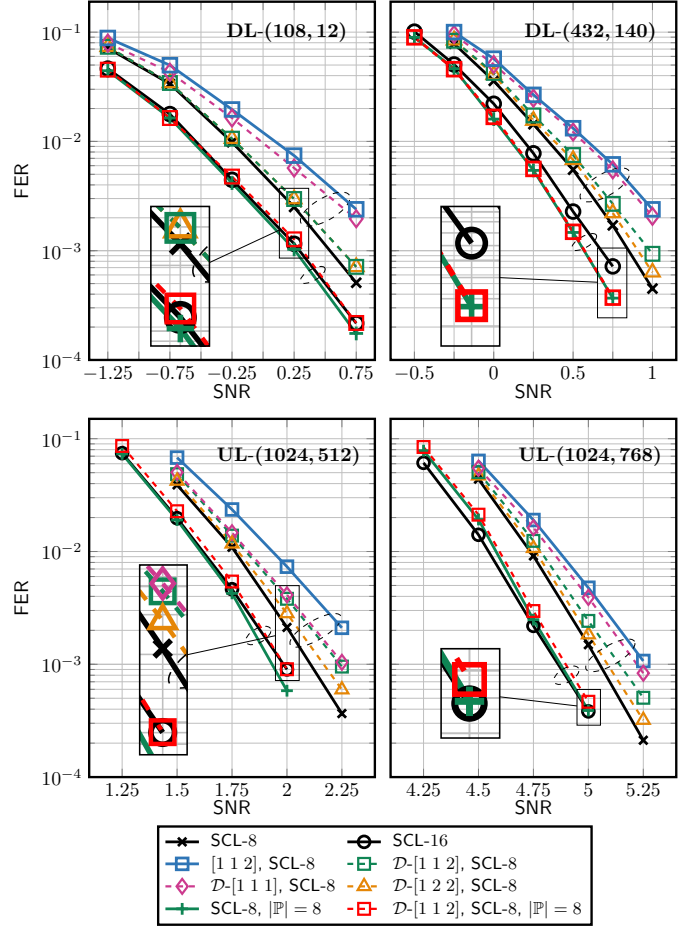


Fig. 9. Quantized FER performance of SCL decoding with different configurations.

number of path forks [11].³ Numerical results demonstrate that a reasonable value for T can significantly reduce decoding latency with negligible error-rate performance degradation [14]. Therefore, an R1 node takes up to $T + 1$ CCs, and an SPC/TYPE-III node needs an extra CC for Wagner decoding to first check for the global/even parity-check constraint, thus leading to a latency of $T + 2$ CCs. In terms of the SR nodes, the RSU takes a fixed two CCs to perform the $|\mathcal{S}|L \rightarrow L$ large-size sorting [14] (as mentioned in Section II-C). It is noteworthy that the first CAS cycle for the SR(R1) node and the first Wagner decoding for the SR(SPC/TYPE-III) are merged in the RSU to effectively reduce decoding cycles [14].⁴

B. S_1 : Dynamic Overlapped Processing of SR Nodes

In this section, we introduce the S_1 strategy, a dynamic overlapped processing for efficiently decoding time-consuming SR nodes by exploiting the independence of the RSU from the BNU. Fig. 8(a) illustrates a partial decoding schedule running over an SR(SPC) node for Frame 0 and Frame 1. According to the alternating fashion, Frame 1 needs to wait for the idle NPU

³The accurate number of path forks equals to $\min(T, K_s)$, where K_s is the number of unfrozen bits in the node.

⁴We use the term SR(R1/SPC/TYPE-III) to denote the SR node with a source node of R1/SPC/TYPE-III.

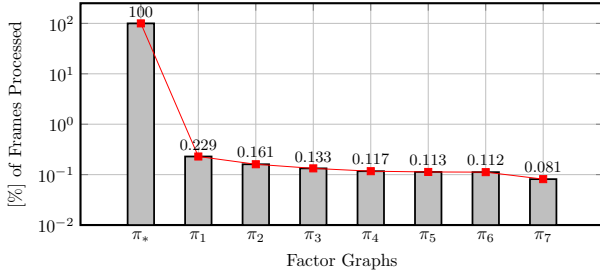


Fig. 10. Percentage histogram of frames processed by each factor graph using SCL-8 decoding with \mathcal{D} -[1, 1, 2], $|\mathbb{P}| = 8$ for UL-(1024, 512).

until Frame 0 completes the SR(SPC) node processing, leading to a delay of 4 CCs. However, as mentioned in Section III-A, the NPU consists of two units that are separated by a pipeline stage: the RSU and the BNU. By pre-loading Frame 1 to the RSU to decode the low-rate part of the SR(SPC) node, concurrent with path forking of Frame 0 in the BSU, two stalls CCs of Frame 1 can thus be saved. Note that the \mathcal{S}_1 strategy is contingent upon two conditions to execute: ① the processing node must be an SR node, ② \mathcal{S}_1 must not bring new delays. Namely, ensuring that the current NPU processing delays are at least 2 CCs so that the RSU can overlap with these delays. Consequently, the \mathcal{S}_1 strategy effectively reduces stalls without any error-rate performance degradation, decreasing the overall latency by 5% for UL-(1024, 512) polar code compared to the original frame-interleaving design [26].

C. \mathcal{S}_2 : Dynamic Path Forking for High-Rate Nodes

To further eliminate residual stalls in our frame-interleaving SCL decoder, we propose an additional optimization called the \mathcal{S}_2 strategy. This method dynamically reduces stalls resulting from the path forking of high-rate nodes while maximizing the number of path forks during periods when the SCU is busy. This approach carefully balances latency reduction with minimal impact on performance. As shown in the example schedule of Fig. 8(c), Frame 0 reduces its path forks by two, and Frame 1 by one, for the SR(SPC) node, collectively achieving a 3-CC reduction compared to the \mathcal{S}_1 strategy. Note that while the \mathcal{S}_2 strategy offers a notable reduction in latency, it does not allow for an infinite reduction in path forking. Herein, we introduce a lower bound on path forking for special nodes to guarantee minimum numbers of path forks in the \mathcal{S}_2 strategy. This constraint ensures that our decoder maintains an acceptable level of performance degradation, which is discussed below.

We define a vector $\mathcal{T} = [T_{R1}, T_{SPC}, T_{TYPE-III}]$ to denote the empirical number of path forks for R1, SPC, and TYPE-III nodes, including SR nodes using these as source nodes. It is noteworthy that [14] demonstrates that a default setting of $\mathcal{T} = [2, 3, 3]$ is a very good latency-performance trade-off for baseline SCL-8 decoding. Then, Fig. 9 illustrates the quantized FER performance for SCL decoding across different \mathcal{T} for DL and UL codes, where \mathcal{D} - \mathcal{T} denotes the \mathcal{S}_2 strategy with \mathcal{T} as its lower bound. In this work, we utilize a sign-magnitude quantization with the 6-bit LLRs and 7-bit PMs, which has

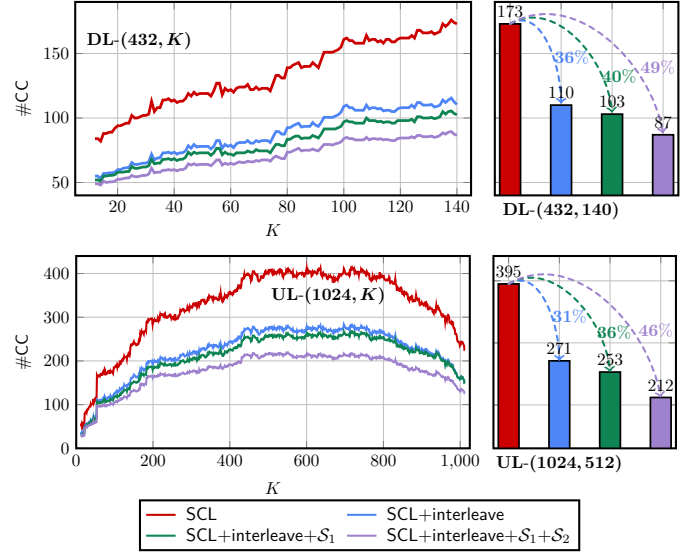


Fig. 11. Average latency analysis of different SCL decoders for DL-(432, K) and UL-(1024, K) codes with $L = 8$, where the baseline SCL refers to [14].

a negligible FER performance loss compared to floating-point. Fig. 9 reveals that the error-correcting performance gap widens as the lower bound decreases (i.e., reducing more path forking), relative to baseline SCL-8 decoding. To obtain an optimal latency-performance balance, the \mathcal{D} -[1, 1, 2] configuration emerges as the preferred choice, with a performance loss of less than 0.15 dB across all simulations. This dynamic configuration retains more path forks than the static [1, 1, 2] setup, offering a notable performance advantage with the same latency. Specifically, for DL-(432, 140) codes, SCL-8 decoding using \mathcal{D} -[1, 1, 2] surpasses the static [1, 1, 2] configuration by approximately 0.25 dB. This improvement is attributed to 35% more path forks by the \mathcal{S}_2 strategy without causing additional stalls. For graph ensemble decoding with 8 graphs, \mathcal{D} -[1, 1, 2] incurs a minor performance loss, but still maintains comparable error-correcting capacity to SCL-16 decoding in Fig. 9. Moreover, Fig. 10 illustrates a percentage histogram of frames processed by each factor graph using SCL-8 decoding with \mathcal{D} -[1, 1, 2], $|\mathbb{P}| = 8$ for UL-(1024, 512) when the target FER is 10^{-3} . After the OFG, the usage of π_1 is only 0.229%.

D. Decoding Latency Analysis

To assess the latency reductions achieved by our proposed methods across various scenarios, Fig. 11 plots the average decoding cycle count per frame for all message lengths K in DL-(432, K) and UL-(1024, K) with different SCL decoders. Following the approach in Section IV-C, we adopt \mathcal{D} -[1, 1, 2] as the \mathcal{S}_2 configuration in the following latency analysis. When decoding the DL-(432, 140) code, the frame-interleaving architecture alone can achieve a 36% latency reduction over the baseline decoder [14]. Moreover, the \mathcal{S}_1 and \mathcal{S}_2 strategies can further deliver additional latency decreases of 4% and 9%, respectively, nearly cutting the decoding time into half (around 50%) to only 87 CCs. Similarly, for the UL-(1024, 512) code, there is a cumulative latency decrease of

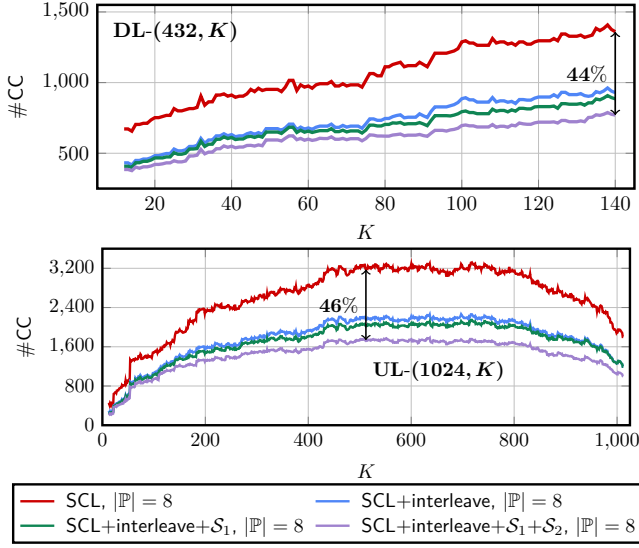


Fig. 12. Worst-case latency analysis of SCL-8 decoders for DL-(432, K) and UL-(1024, K) codes with 8 graphs per frame.

46%, resulting in only 212 CCs per frame on average. These results underscore the positive impact of our optimization strategies across various code rates and lengths, which nearly achieve the ideal target of the proposed architecture (i.e., time-sharing two computational units, filling all idle slots). Fig. 12 illustrates the worst-case latency for graph ensemble decoding. When handling 8 graphs, the baseline SCL-8 decoder typically suffers from an 8-fold increase in latency (indicated by the red line). However, with the proposed decoder, we can reduce the worst-case latency by 44% and 46% for DL-(432, 140) and UL-(1024, 512) codes, respectively.

V. ONLINE INSTRUCTION GENERATOR

Node-based polar decoders rely on identifying the types and lengths of special nodes. This necessitates complex control logic. To bypass this issue, most decoders perform this identification offline and then store the resulting instructions in dedicated memories. The decoder then proceeds by reading these instructions to coordinate each component. However, this method incurs significant area overhead for storing instructions and makes it almost impossible to rapidly change the rate as required by 5G [14], [33]. Note that these instructions are closely tied to N and K , and any changes to these parameters require a new list of instructions. As the range of message lengths is from 12 to 1706 in 5G NR polar codes, this offline generation can not be precomputed for all relevant code configurations. Moreover, given the complexity of our frame-interleaving decoder, we also support three distinct working modes, graph ensemble decoding, generalized SR nodes, and multiple dynamic processing strategies to optimize the performance and latency. These factors strongly motivate the design of an online instruction generator to enable the required flexibility.

In this section, we design an online instruction generator tailored to work synchronously with the decoder to identify basic nodes and generalized SR nodes and generate the corresponding instructions on-the-fly. Instead of storing a bit-

channel reliability vector as in [25], our generator operates directly with the binary sequence defining the information bits \mathbb{A} (or \mathbb{A}' for PFGs).⁵ It features a sliding window of maximum node size $N_{s_{\max}}$, moving along the sequence \mathbb{A} . This window contains a sub-sequence \mathbb{A}_{sub} , enabling the identification of special nodes at varying lengths within \mathbb{A}_{sub} , to progress until the entire sequence \mathbb{A} is analyzed.

A. Node Identification for Basic Nodes

Given the frozen bit patterns of the five basic nodes described in Section II-C, we group the basic nodes as $\{\text{R0}, \text{REP}\}$ (special cases of generalized REP nodes [9]) and $\{\text{R1}, \text{SPC}, \text{TYPE-III}\}$ (special cases of generalized parity-check nodes [9]), as each group shares similar patterns for their node recognition independent of their length. Hence, we employ a unified logic for each group in pursuit of area saving. We define a symbol \mathcal{M}_X^k to track whether a length- 2^k special node “X” is detected or not in the sub-sequence \mathbb{A}_{sub} corresponding to the sliding window, where “X” means the node type and $\log N_{s_{\min}} \leq k < \log N_{s_{\max}}$. For the $\{\text{R0}, \text{REP}\}$ group, the control logic can be mathematically formulated as

$$\begin{aligned} \mathcal{M}_{\text{R0}}^{k+1} &= \begin{cases} 1, & \text{if } \mathcal{M}_{\text{R0}}^k = 1 \text{ and } \mathbb{A}_{\text{sub}}[2^{k+1}-1] = 0 \text{ and } \xi, \\ 0, & \text{otherwise,} \end{cases} \\ \mathcal{M}_{\text{REP}}^{k+1} &= \begin{cases} 1, & \text{if } \mathcal{M}_{\text{REP}}^k = 1 \text{ and } \mathbb{A}_{\text{sub}}[2^{k+1}-1] = 1 \text{ and } \xi, \\ 0, & \text{otherwise,} \end{cases} \end{aligned} \quad (6)$$

where ξ represents the common logic $\mathbb{A}_{\text{sub}}[2^k : 2^{k+1}-2] = 0$ and $k \geq 1$. The associated logic gates are shared by the identification of R0 and REP, thus reducing the overall logic area. Subsequently, the identification logic of the $\{\text{R1}, \text{SPC}, \text{TYPE-III}\}$ group is formulated as

$$\begin{aligned} \mathcal{M}_{\text{R1}}^{k+1} &= \begin{cases} 1, & \text{if } \mathcal{M}_{\text{R1}}^k = 1 \text{ and } \zeta, \\ 0, & \text{otherwise,} \end{cases} \\ \mathcal{M}_{\text{SPC}}^{k+1} &= \begin{cases} 1, & \text{if } \mathcal{M}_{\text{SPC}}^k = 1 \text{ and } \zeta, \\ 0, & \text{otherwise,} \end{cases} \\ \mathcal{M}_{\text{TYPE-III}}^{k+1} &= \begin{cases} 1, & \text{if } \mathcal{M}_{\text{TYPE-III}}^k = 1 \text{ and } \zeta, \\ 0, & \text{otherwise,} \end{cases} \end{aligned} \quad (7)$$

where ζ represents the common logic $\mathbb{A}_{\text{sub}}[2^k : 2^{k+1}-1] = 1$, $k \geq 1$ for $\mathcal{M}_{\text{R1}}^k$ and $\mathcal{M}_{\text{SPC}}^k$, and $k \geq 2$ for $\mathcal{M}_{\text{TYPE-III}}^k$ since length-2 TYPE-III node is invalid. Thus, we can identify the basic nodes at all possible lengths by recursively invoking (6) and (7). Note that some preconditions are necessary to trigger the above recursive processing. For instance, (8) illustrates the preconditions of the $\{\text{R1}, \text{SPC}, \text{TYPE-III}\}$ group.⁶

$$\begin{aligned} \mathcal{M}_{\text{R1}}^1 &= \begin{cases} 1, & \text{if } \mathbb{A}_{\text{sub}}[0:1] = 1, \\ 0, & \text{otherwise,} \end{cases} \\ \mathcal{M}_{\text{SPC}}^1 &= \begin{cases} 1, & \text{if } \mathbb{A}_{\text{sub}}[0:1] = [0, 1], \\ 0, & \text{otherwise,} \end{cases} \\ \mathcal{M}_{\text{TYPE-III}}^2 &= \begin{cases} 1, & \text{if } \mathbb{A}_{\text{sub}}[0:3] = [0, 0, 1, 1], \\ 0, & \text{otherwise.} \end{cases} \end{aligned} \quad (8)$$

⁵For brevity, we still represent the binary sequence vector of the information set as \mathbb{A} , where $\mathbb{A}[i]$ indicates a frozen bit if 0 and an information bit as 1.

⁶The preconditions of the $\{\text{R0}, \text{REP}\}$ group are similar to (8). Hence, we omit them in this paper for brevity.

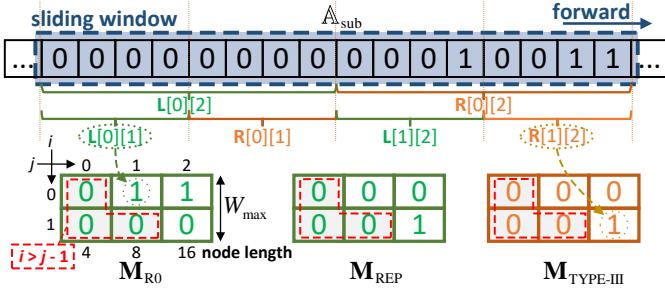


Fig. 13. Representation of the 2D arrays describing the locations of three basic nodes (R0, REP, and TYPE-III) in the example 16-bit sequence A_{sub} , where the horizontal index represents the stage of the basic node ($j - i + 1$) and the vertical index represents the basic node length (2^{j-i+1}). The “left” and “right” segments in A_{sub} are labeled green and orange, respectively.

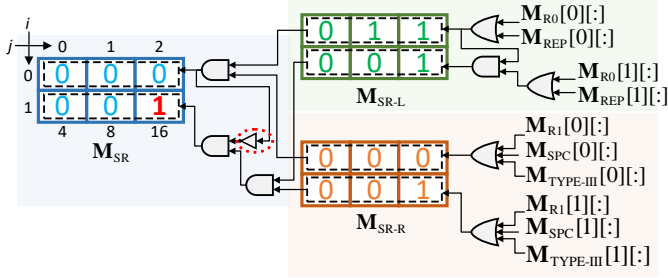


Fig. 14. The regrouping process for SR nodes, using the 2D arrays of basic nodes.

B. Node Identification for SR Nodes

As outlined in Section II-C, the identification of SR nodes is more complicated than that of the basic nodes since the SR node has a generalized structure and requires a recursive detection process. To effectively tackle this challenge, we divide the detection logic for SR nodes into three phases:

- 1) Detection of the “left” low-rate part within SR nodes is responsible for identifying R0 and REP nodes located in the left regions of SR nodes at different stages.
- 2) Detection of the “right” high-rate part within SR nodes is responsible for identifying R1, SPC, and TYPE-III nodes as the source node in the right regions of SR nodes at different stages of the decoding tree.
- 3) The “regrouping” phase prioritizes selecting the SR node with the maximum length and, as a secondary criterion, the source node of the longest feasible length.

In Fig. 13, we depict an example SR node using a 16-bit sequence A_{sub} in the sliding window. In this case, we assume $N_{s_{\text{max}}} = 16$ and $W_{\text{max}} = 2$, where W_{max} denotes the maximum number of R0/REP nodes as left descendants. We first define a two-dimensional (2D) array, M_X , per basic node type “X” to find the locations of all node candidates. The dimension of this 2D is $W_{\text{max}} \times (\log N_{s_{\text{max}}} - 1)$, the same for all basic node types. The horizontal index i reveals the stage of the basic node, and the vertical index j reveals the basic node length. For instance, a pair of $\{i, j\}$ represents a length- 2^{j-i+1} basic node that is located at the $j - i + 1$ -th stage,

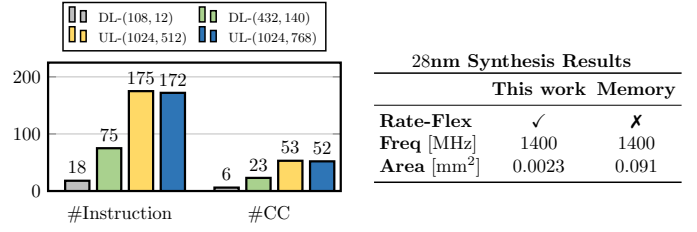


Fig. 15. Implementation results of our instruction generator.

$0 \leq i \leq W_{\text{max}} - 1$ and $0 \leq j < \log N_{s_{\text{max}}} - 1$. Note that each index pair, $\{i, j\}$, not only provides the position of the basic node itself, but also indicates a potential constraint of the SR node where the basic node can be located: the number of identified left-side R0/REP nodes is $i + 1$, the length of the SR node is $N_s = 2^{j+2}$, and the length of the source node is $N_r = 2^{j-i+1}$. It is noteworthy that such a structure of M (for basic nodes) does not imply that it can only be populated once the SR nodes are successfully identified. Instead, the 2D array M can be filled as long as the basic node of length- 2^{j-i+1} is detected under the SR constraint of each index pair $\{i, j\}$ (herein, the identification of basic nodes follows (6–8) as described in Section V-A).

To facilitate the detection of the “left” and “right” parts within SR nodes, we label the segments of A_{sub} as $L[i][j]$ or $R[i][j]$, as depicted in Fig. 13.⁷ In phase 1, we check the L segments to identify R0 and REP nodes and then fill M_{R0} and M_{REP} . To be specific, $M_{R0}[0][1] = 1$ because a length-4 R0 node is found in the left segment $L[0][1]$. Similarly, in phase 2, we check the R segments to identify high-rate source nodes and populate M_{R1} , M_{SPC} , and $M_{TYPE-III}$. For example, $M_{TYPE-III}[1][2] = 1$ because a length-4 TYPE-III node is found in the right segment $R[1][2]$. The arrays of R1 and SPC nodes can be generated similarly, yet, with all zeros in this example. Note that the red dashed rectangle on a gray background represents a zone without an SR node structure. This area is directly marked as 0, reflecting that the source node is at its minimum length and that N_s must exceed N_r .

For phase 3, “regrouping” is introduced in Fig. 14 to extract the longest SR node that incorporates the source node of maximum length. Herein, three new 2D arrays, M_{SR-L} , M_{SR-R} , and M_{SR} , are constructed, by aggregating the M of basic nodes through simple combinatorial logic. Note that the entire SR node detection is from the top down. For M_{SR-L} , the process begins with a straightforward bit-wise OR operation for $M_{R0}[0][:]$ and $M_{REP}[0][:]$ at the horizontal index $i = 0$. For the subsequent stage, $i = 1$, an additional AND gate with the vector from the previous stage is performed. This step ensures that a left-part low-rate node at the current stage is considered in the SR node only if R0/REP nodes have been identified at all previous source node stages. This recursive approach can continue if W_{max} exceeds 2. On the other hand, M_{SR-R} is formed through a simple bit-wise OR operation among M_{R1} , M_{SPC} , and $M_{TYPE-III}$. The final step involves M_{SR} , which

⁷Based on the SR node structure, the left segment $L[i][j]$ is merely used to detect the R0 and REP nodes and the right segment $R[i][j]$ only for the R1, SPC, and TYPE-III nodes.

searches positions where both M_{SR-L} and M_{SR-R} are marked with “1”, indicating the presence of SR nodes. Notably, the NOT gate highlighted by a red dashed circle reveals that an SR node with a shorter source node will be activated only if no source node of greater length is available. In this case, we obtain the only SR node in $M_{SR}[1][2] = 1$, based on which, we detect a length-16 SR node with a length-4 TYPE-III node as its source node, corresponding to the $N_{4,1}$ depicted in Fig. 1. If more than one valid SR node is found in M_{SR} , we give priority to the one with the longest length (i.e., the upper right corner of the array M_{SR} enjoys a higher priority).

C. Hardware Results of Online Instruction Generator

While operating continuously, our proposed online instruction generator can identify one node and generate the corresponding series of instructions regarding this node in each CC. For each node ultimately identified (only if the SR structure does not exist, we then consider basic node types), at least two instructions are generated: one for the SCU and one for the NPU. As illustrated in Fig. 15, our instruction generator only requires 53 CCs (i.e., one node per cycle) to complete the generation of 175 instructions required for UL-(1024, 512) (the worst-case in UL). To prevent overloading the decoder cores with a considerable number of instructions at multiple CCs, which would exceed its processing capacity, we have integrated a compact FIFO buffer between the decoder cores and the controller, as shown in Fig. 2. This buffer temporarily holds the newly generated instructions, pausing further node identification when the FIFO fills up. To highlight the advantages of our online instruction generator, we compared it with a straightforward instruction memory [14] that holds instructions generated offline, providing a capacity of 175 instructions (i.e., the demand for UL-(1024, 512)). Given that two interleaved frames are decoded simultaneously, the required memory capacity further doubles. Synthesis results in 28nm FD-SOI technology show our online generator occupies only an area of 0.0023 mm². This area is 97.5% smaller and enjoys a comparable data path length compared to straightforward instruction memory. Crucially, our approach supports on-the-fly instruction generation, enabling decoder rate flexibility.

VI. IMPLEMENTATION RESULTS

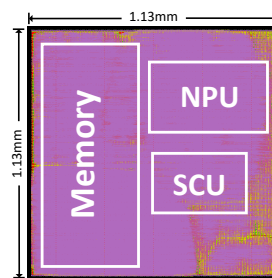
In this section, we present the implementation results of our generalized node-based SCL decoder with frame-interleaving, based on a STM 28nm FD-SOI technology. The decoder is synthesized with Synopsys Design Compiler and placed and routed using Cadence Innovus. Power analysis is done under typical operating conditions with parasitic and activity back annotation (1.0 V and 25°C). We follow the default configurations of [14] to fix the number of SCU stages (#SCU) to 3, the number of PEs at the first stage of the SCU (#PE) to 64, and the maximum size of nodes to $N_{s_{max}} = 32$. We select $W_{max} = 2$ as the best trade-off between decoding time and area (i.e., node identification of Section V can identify the SR nodes with at most two R0/REP left descendants). Moreover, as length-32 SR nodes are rarely found in 5G NR polar codes, we constrain the RSU size to 16. To strike a

TABLE I
IMPLEMENTATION RESULTS OF OUR DECODERS[†].

	This work [‡]				TSP'22 [14]			
	512		1024		512		1024	
Length [bit]	4	8	4	8	4	8	4	8
List-size	76	87	188	212	155	173	355	395
CCs	0.064	0.089	0.161	0.22	0.119	0.174	0.28	0.40
Latency [μ s]	0.327	0.648	0.425	0.838	0.211	0.439	0.286	0.608
Area [mm ²]	1181	970	1168	965	1302	994	1255	977
Freq. [MHz]								
Coded T/P [Gbps]	7.956	5.709	6.362	4.661	4.301	2.942	3.619	2.532
T/P gain	↑85%	↑94%	↑76%	↑84%	—	—	—	—
Area Eff. [Gbps/mm ²]	24.33	8.81	14.97	5.56	20.43	6.704	12.67	4.165
Area Eff. gain [†]	↑19%	↑32%	↑18%	↑34%	—	—	—	—

[†] While our works are compatible with all DL and UL codes, latency is obtained at DL-(432, 140) and UL-(1024, 512) codes for length-512 and length-1024 decoders, respectively.

[‡] We set the decoder to Mode-III for enhanced average T/P and reliability.



Technology	28nm FD-SOI
Quantization [bit]	6
Core Area [mm ²]	1.13 × 1.13
Gate Count [M]	1.45
Voltage [V]	1.0
Frequency [MHz]	692
Coded T/P [Gbps]	3.34
Power [mW]	201.6
Energy [pJ/bit]	60.32

Fig. 16. A post-layout of our length-1024 SCL decoder with $L = 8$ implemented in a 28nm process, wherein the white boxes represent the memory and two computational units, the SCU and the NPU.

balance between error-correcting performance and hardware complexity, as shown in Fig. 9, we employ a sign-magnitude quantization with the 6-bit LLRs and 7-bit PMs. This choice incurs a negligible FER performance loss compared to floating point. Note that we present two versions of our decoder, one tailored to DL with a maximum code length of 512 and one for UL with a maximum code length of 1024 bits.

A. Implementation Results of Our Decoder

Table I summarizes the synthesis results of our proposed decoder tailored for DL and UL polar codes with $L \in \{4, 8\}$. While our decoders are compatible with all 5G NR polar codes, the latency of Table I focuses on two classical codes: DL-(432, 140) and UL-(1024, 512). In comparison with the baseline decoder [14], our length-512 decoder with $L = 8$ yields a 47.6% area increase (attributed to two memory instances for interleaving) yet significantly reduces the worst-case latency from 173 cycles to 87 cycles (nearly half). Moreover, since the various working modes (see Section III) and the dynamic strategies to eliminate stalls (see Section IV) are only involved with the control signal interactions, our work shares a comparable critical path and a similar maximum frequency with the baseline decoder. Consequently, our length-512 decoder with $L = 8$ attains a throughput of 5.709 Gbps and an area efficiency of 8.81 Gbps/mm², surpassing [14] by 94% and 32%, respectively. For length-1024 codes at half rate, while our decoder has a 37.8% increase in cell area to 0.838 mm²,

TABLE II
COMPARISONS WITH THE STATE-OF-THE-ART SCL DECODERS FOR THE UL-(1024, 512) CODE.

	This work		JETCAS'17 [6]	ISWCS'18 [31]	JSSC'20 [34]	VLSI'22 [35]	TCAS-I'23 [15]	ISTC'23 [‡] [19]	TSP'15 [4]	TSP'17 [11]	TSP'22 [14]
Technology [nm]	28		28	16	40	28	65	12	90	65	28
Implementation	Synthesis	Post-layout	Silicon	Silicon	Silicon	Silicon	Post-layout	Post-layout	Synthesis	Synthesis	Synthesis
Full 5G NR	✓		✗	✓	✓	✓	✓	✗	✗	✗	✓
Permutations [◊]	✓		✗	✗	✗	✗	✗	✓	✗	✗	✗
Rate-Flexible	✓		✓	✓	✓	✗	✗	✗	✓	✗	✗
Voltage [V]	1.0		1.3	0.9	0.9	1.05	1.1	0.8	1.0	—	1.0
List-size	8		4	8	2	8	8	8	8	8	8
CCs	212		2408	790	136	454	304	—	2662	618	395
SNR@FER = 10 ⁻³	1.98		2.3	2.1	2.63	2.1	2.1	3.05	2.1	2.1	2.1
Latency [μ s]	0.22	0.306	3.34	0.72	0.32	1.10	1.003	0.064	4.18	0.85	0.40
Area [mm^2]	0.838	1.28	0.44	0.06	0.637	0.595	3.89	0.381	3.58	3.975	0.608
Frequency [MHz]	965	692	721	1100	430	413	300	500	637	722	977
Coded T/P [Gbps]	4.661	3.34	0.307	1.426	3.25	0.925	1.02	64.0	0.246	1.198	2.532
Power [mW]	—	201.6	128.3	—	42.8	101.4	389	552	—	—	—
Scaled to 28nm, 1.0 V [†]											
Area [mm^2]	0.838	1.28	0.44	0.184	0.312	0.595	0.722	2.074	0.347	0.738	0.608
Coded T/P [Gbps]	4.661	3.34	0.307	0.815	4.643	0.925	2.368	27.43	0.791	2.781	2.532
Area Eff. [Gbps/ mm^2]	5.56	2.62	0.692	4.435	14.87	1.56	3.28	13.24	2.282	3.77	4.165
Power [mW]	—	201.6	75.92	—	52.84	91.97	321.49	862.5	—	—	—
Energy [pJ/bit]	—	60.32	247.3	—	11.38	99.43	135.77	31.44	—	—	—

[†] Scaled to 28nm and 1.0 V with area $\propto \sigma^2$, frequency $\propto 1/\sigma$, and power $\propto 1/u^2$, where σ is the scaling factor to 28nm and u is the scaling factor to 1.0 V.

[‡] Only [19] is implemented for (128, 60) codes while the others are for (1024, 512) polar codes.

[◊] Our work supports graph ensemble decoding and [19] uses automorphisms to enhance error-rate performance.

it delivers an 84% increase to 4.661 Gbps in throughput and improves area efficiency by 34% to 5.56 Gbps/ mm^2 .

Fig. 16 depicts the post-layout results of our length-1024 SCL-8 decoder. When all the physical design steps are completed, the post-layout of our decoder reveals a core size of $1.13 \times 1.13 \text{ mm}^2$ with a cell utilization of 65.6%. Due to the effects of the physical wire lengths and parasitic delays, the maximum operating frequency is reduced to 692 MHz. When decoding UL-(1024, 512) code with a throughput of 3.34 Gbps, this decoder has a dynamic power consumption of 201.6 mW and an energy consumption of 60.32 pJ/bit.

B. Comparison with Previous Works

Table II provides a comprehensive comparison between our frame-interleaving decoder and the state-of-the-art polar decoder implementations in [4], [6], [11], [14], [15], [19], [31], [34], [35]. To ensure fairness, we normalize all previous works to a 28 nm process with a supply voltage of 1.0 V.⁸ Compared to a similar node-based SCL decoder with the same 28 nm technology [35], our work has a $3.61\times$ throughput, $1.68\times$ area efficiency, and 39.3% less energy consumption. When compared to conventional SCL decoder without node-based techniques [6], [34], our decoder enjoys a throughput that is $10.89\times$ faster than [6] and $4.10\times$ higher than [31]. Compared to the SCL decoder with overlapped operation units in [15] that leverages parallel processing, our work has a 30.2% reduction of decoding latency to only 212 CCs per frame when decoding the UL-(1024, 512) code. Although our area efficiency is 20.1% inferior to that of [15], we present a 41.1% higher throughput and achieve a 55.6% lower energy consumption. In addition, our decoder supports graph ensemble decoding (in

Mode-II and Mode-III), thus improving the error-correcting performance by 0.18 dB at an FER of 10^{-3} (identical to SCL-16 decoding shown in Fig. 9). While our area efficiency and energy efficiency are inferior to the SC automorphism list (SCAL) decoder in [19], given that [19] is mainly restricted to short-length codes and hard-wired routing networks, our decoder is fully compatible with all 5G NR polar codes and supports a flexible permutation generator. Compared to [19], our decoder has a 76.6% lower power consumption. It is noteworthy that the integrated online instruction generator contributes to the rate-flexibility of our decoder, which is not achieved by the previous node-based works [11], [14], [15], [35] mentioned above. Moreover, our proposed decoder supports two frames/graphs decoding simultaneously, given that $2\times$ can achieve reasonable improvements for 5G scenarios. This work can also be extended to multiple cores for higher parallelism.

VII. CONCLUSION

The architecture of frame-interleaving significantly enhances the efficiency of node-based SCL decoders by eliminating processing delays from data-dependent computational units. This improvement is achieved by reusing otherwise idle processing units to decode two frames simultaneously. However, simple interleaving retains some residual stalls. Our dynamic stall-reduction strategies effectively remove these stalls by reasonably reorganizing the decoding schedule, allowing for considerable overlapped operations without architectural modifications. Moreover, our frame-interleaving decoder supports graph ensemble decoding and various modes of operation aiming at higher throughput, performance, and efficiency. We also introduce an online instruction generator, tailored to SR nodes, that ensures low decoding latency and rate flexibility in our generalized node-based SCL decoder. The corresponding

⁸The technology scaling method refers to Table I of [36]. Note that this is rough and optimistic since it does not apply to the interconnects [37], [38].

28nm FD-SOI ASIC decoder with $L = 8$ demonstrates that our work has a throughput of 3.34 Gbps and an area efficiency of 2.62 Gbps/mm² for the UL-(1024, 512) code.

REFERENCES

- [1] E. Arkan, "Channel polarization: A method for constructing capacity-achieving codes for symmetric binary-input memoryless channels," *IEEE Trans. Inf. Theory*, vol. 55, no. 7, pp. 3051–3073, July 2009.
- [2] *Chairman's notes of agenda item 7.1.5 Channel coding and modulation*, 3GPP TSG RAN WG1 meeting #87, R1-1613710, Nov. 2016.
- [3] I. Tal and A. Vardy, "List decoding of polar codes," *IEEE Trans. Inf. Theory*, vol. 61, no. 5, pp. 2213–2226, May 2015.
- [4] A. Balatsoukas-Stimming, M. Bastani Parizi, and A. Burg, "LLR-based successive cancellation list decoding of polar codes," *IEEE Trans. Signal Process.*, vol. 63, no. 19, pp. 5165–5179, Oct. 2015.
- [5] *Final Report of 3GPP TSG RAN WG1 #AH1_NR v1.0.0*, 3GPP TSG RAN WG1 meeting #88, R1-1701553, Feb. 2017.
- [6] P. Giard, A. Balatsoukas-Stimming, T. C. Müller, A. Bonetti, C. Thibault, W. J. Gross, P. Flatresse, and A. Burg, "PolarBear: A 28-nm FD-SOI ASIC for decoding of polar codes," *IEEE J. Emer. Top. Circuits Syst.*, vol. 7, no. 4, pp. 616–629, Dec. 2017.
- [7] G. Sarkis, P. Giard, A. Vardy, C. Thibault, and W. J. Gross, "Fast polar decoders: Algorithm and implementation," *IEEE J. Sel. Areas Commun.*, vol. 32, no. 5, pp. 946–957, May 2014.
- [8] M. Hanif and M. Ardakani, "Fast successive-cancellation decoding of polar codes: Identification and decoding of new nodes," *IEEE Commun. Lett.*, vol. 21, no. 11, pp. 2360–2363, Nov. 2017.
- [9] C. Condo, V. Bioglio, and I. Land, "Generalized fast decoding of polar codes," in *Proc. IEEE Glob. Commun. Conf. (GLOBECOM)*, 2018, pp. 1–6.
- [10] G. Sarkis, P. Giard, A. Vardy, C. Thibault, and W. J. Gross, "Fast list decoders for polar codes," *IEEE J. Sel. Areas Commun.*, vol. 34, no. 2, pp. 318–328, Nov. 2016.
- [11] S. A. Hashemi, C. Condo, and W. J. Gross, "Fast and flexible successive-cancellation list decoders for polar codes," *IEEE Trans. Signal Process.*, vol. 65, no. 21, pp. 5756–5769, Nov. 2017.
- [12] M. Hanif, M. H. Ardakani, and M. Ardakani, "Fast list decoding of polar codes: Decoders for additional nodes," in *Proc. IEEE Wireless Commun. Netw. Conf. Workshops (WCNC)*, 2018, pp. 37–42.
- [13] H. Zheng, S. A. Hashemi, A. Balatsoukas-Stimming, Z. Cao, T. Koonen, J. M. Cioffi, and A. Goldsmith, "Threshold-based fast successive cancellation decoding of polar codes," *IEEE Trans. Commun.*, vol. 69, no. 6, pp. 3541–3555, Jun. 2021.
- [14] Y. Ren, A. T. Kristensen, Y. Shen, A. Balatsoukas-Stimming, C. Zhang, and A. Burg, "A sequence repetition node-based successive cancellation list decoder for 5G polar codes: Algorithm and implementation," *IEEE Trans. Signal Process.*, vol. 70, no. 6, pp. 5592–5607, Oct. 2022.
- [15] D. Kam, B. Y. Kong, and Y. Lee, "Low-latency SCL polar decoder architecture using overlapped pruning operations," *IEEE Trans. Circuits Syst. I*, vol. 70, no. 3, pp. 1417–1427, Jan. 2023.
- [16] M. Geiselhart, A. Elkelesh, M. Ebada, S. Cammerer, and S. ten Brink, "On the automorphism group of polar codes," in *Proc. IEEE Int. Symp. Inf. Theory (ISIT)*, 2021, pp. 1230–1235.
- [17] —, "Automorphism ensemble decoding of Reed-Muller codes," *IEEE Trans. Commun.*, vol. 69, no. 10, pp. 6424–6438, Jul. 2021.
- [18] C. Kestel, M. Geiselhart, L. Johannsen, S. ten Brink, and N. Wehn, "Automorphism ensemble polar code decoders for 6G URLLC," in *Proc. IEEE Conf. System. Commun. Coding (SCC)*, 2023, pp. 1–6.
- [19] L. Johannsen, C. Kestel, M. Geiselhart, T. Vogt, S. Ten Brink, and N. Wehn, "Successive cancellation automorphism list decoding of polar codes," in *Proc. IEEE Int. Symp. Topics Coding (ISTC)*, 2023, pp. 1–5.
- [20] A. Elkelesh, M. Ebada, S. Cammerer, and S. ten Brink, "Belief propagation list decoding of polar codes," *IEEE Commun. Lett.*, vol. 22, no. 8, pp. 1536–1539, Aug. 2018.
- [21] Y. Ren, Y. Shen, Z. Zhang, X. You, and C. Zhang, "Efficient belief propagation polar decoder with loop simplification based factor graphs," *IEEE Trans. Veh. Technol.*, vol. 69, no. 5, pp. 5657–5660, Mar. 2020.
- [22] Y. Ren, Y. Shen, L. Zhang, A. T. Kristensen, A. Balatsoukas-Stimming, E. Boutillon, A. Burg, and C. Zhang, "High-throughput and flexible belief propagation list decoder for polar codes," *IEEE Trans. Signal Process.*, vol. 72, pp. 1158–1174, Feb. 2024.
- [23] N. Doan, S. A. Hashemi, M. Mondelli, and W. J. Gross, "On the decoding of polar codes on permuted factor graphs," in *Proc. IEEE Global Commun. Conf. (GLOBECOM)*, 2018, pp. 1–6.
- [24] S. A. Hashemi, C. Condo, and W. J. Gross, "A fast polar code list decoder architecture based on sphere decoding," *IEEE Trans. Circuits Syst. I*, vol. 63, no. 12, pp. 2368–2380, Dec. 2016.
- [25] S. A. Hashemi, C. Condo, M. Mondelli, and W. J. Gross, "Rate-flexible fast polar decoders," *IEEE Trans. Signal Process.*, vol. 67, no. 22, pp. 5689–5701, Nov. 2019.
- [26] L. Zhang, Y. Ren, Y. Shen, W. Zhou, A. Balatsoukas-Stimming, C. Zhang, and A. Burg, "A low-latency and high-performance SCL decoder with frame-interleaving," in *Proc. IEEE Int. Symp. Circuits Syst. (ISCAS)*, 2024, pp. 1–5.
- [27] *5G NR: Multiplexing and channel coding*, 3GPP TS 38.212 version 15.2.0, July 2018.
- [28] S. A. Hashemi, N. Doan, M. Mondelli, and W. J. Gross, "Decoding Reed-Muller and polar codes by successive factor graph permutations," in *Proc. IEEE Int. Symp. Topics Coding (ISTC)*, 2018, pp. 1–5.
- [29] G. Marvin, A. Elkelesh, M. Ebada, S. Cammerer, and S. ten Brink, "CRC-aided belief propagation list decoding of polar codes," in *Proc. IEEE Int. Symp. Inf. Theory (ISIT)*, 2020, pp. 395–400.
- [30] C. Condo, S. A. Hashemi, A. Ardakani, F. Ercan, and W. J. Gross, "Design and implementation of a polar codes blind detection scheme," *IEEE Trans. Circuits Syst. II*, vol. 66, no. 6, pp. 943–947, June 2019.
- [31] X. Liu, Q. Zhang, P. Qiu, J. Tong, H. Zhang, C. Zhao, and J. Wang, "A 5.16Gbps decoder ASIC for polar code in 16nm FinFET," in *Proc. IEEE Int. Symp. Wireless Commun. Syst. (ISWCS)*, 2018, pp. 1–5.
- [32] M. Geiselhart, F. Krieg, J. Clausius, D. Tandler, and S. ten Brink, "6G: A welcome chance to unify channel coding?" *IEEE BITS Info. Theory Mag.*, pp. 1–12, Oct. 2023.
- [33] Y. Ren, H. Harb, Y. Shen, A. Balatsoukas-Stimming, and A. Burg, "A generalized adjusted min-sum decoder for 5G LDPC codes: Algorithm and implementation," *IEEE Trans. Circuits Syst. I*, vol. 71, no. 6, pp. 2911–2924, Jun. 2024.
- [34] Y. Tao, S.-G. Cho, and Z. Zhang, "A configurable successive-cancellation list polar decoder using split-tree architecture," *IEEE J. Solid-State Circuits*, vol. 56, no. 2, pp. 612–623, Sep. 2020.
- [35] D. Kam, B. Y. Kong, and Y. Lee, "A 1.1μs 1.56 Gb/s/mm² cost-efficient large-list SCL polar decoder using fully-reusable LLR buffers in 28nm CMOS technology," in *Proc. IEEE Symp. VLSI Technol. Circuits*, 2022, pp. 204–205.
- [36] A. Stillmaker and B. Baas, "Scaling equations for the accurate prediction of CMOS device performance from 180 nm to 7 nm," *Integration*, vol. 58, pp. 74–81, 2017.
- [37] S. Yin, P. Ouyang, S. Tang, F. Tu, X. Li, S. Zheng, T. Lu, J. Gu, L. Liu, and S. Wei, "A high energy efficient reconfigurable hybrid neural network processor for deep learning applications," *IEEE J. Solid-State Circuits*, vol. 53, no. 4, pp. 968–982, 2017.
- [38] H. Mo, W. Zhu, W. Hu, Q. Li, A. Li, S. Yin, S. Wei, and L. Liu, "A 12.1 TOPS/W quantized network acceleration processor with effective-weight-based convolution and error-compensation-based prediction," *IEEE J. Solid-State Circuits*, vol. 57, no. 5, pp. 1542–1557, 2021.